Elemental tellurium as a chiral *p*-type thermoelectric material

Hua Peng and Nicholas Kioussis[*]

Department of Physics, California State University Northridge, Northridge, California 91330-8268, USA

G. Jeffrey Snyder

Department of Materials Science, California Institute of Technology, Pasadena, California 91125, USA

The thermoelectric transport properties of elemental tellurium are investigated by density functional theory combined with the Boltzmann transport equation in the rigid band approximation. We find that the thermoelectric transport properties parallel and perpendicular to the helical chains are highly asymmetric (almost symmetric) for *p*- (*n*-) type doped tellurium due to the anisotropic (isotropic) hole (electron) pockets of the Fermi surface. The electronic band structure shows that the *lone-pair* derived uppermost heavy-hole and extremely light-hole lower valence bands offer the opportunity to obtain both a high Seebeck coefficient and electrical conductivity along the chains through Sb or Bi doping. Furthermore, the stairlike density of states yields a large asymmetry for the transport distribution function relative to the Fermi energy which leads to large thermopower. The calculations reveal that tellurium has the potential to be a good *p*-type thermoelectric material with an optimum figure of merit zT of 0.31 (0.56) at room temperature (500 K) at a hole concentration around 1×10^{19} cm^{-3}. Exploiting the rich chemistry of lone pairs in chiral solids may have important implications for the discovery of high-zT polychalcogenide-based thermoelectric materials.

PACS number(s): 73.50.−h, 71.20.Ps, 84.60.Rb

I. INTRODUCTION

Thermoelectric materials can be used to directly convert heat to electricity and vice versa. The performance of a thermoelectric is measured by the figure of merit zT, $zT = S^2 \sigma T / \kappa$, where S is the Seebeck coefficient, σ is the electrical conductivity, $\kappa = \kappa_e + \kappa_L$ the thermal conductivity which includes both the electronic and lattice contributions, and T the absolute temperature. The product $PF = S^2\sigma$ is often referred to as the power factor. S, σ, and κ_e are mainly related to the electronic structure of the material while κ_L primarily depends on the lattice. During the past several years intense research effort has focused on improving the zT for high-energy conversion efficiency in existing complex bulk thermoelectric materials [1–3] (binary and ternary semiconductor alloys) and on identifying promising novel materials.

Achieving higher thermoelectric performance requires high S and σ values and low thermal conductivity. However, the Seebeck coefficient and electrical conductivity are generally inversely related. Thus, optimizing the thermoelectric performance involves balancing these conflicting parameters. It was suggested that a low-dimensional density of states could potentially improve S without reducing σ. Band engineering including high band degeneracy, resonant states, etc., though doping and composition have often been applied to manipulate the thermoelectric performance [4–7]. For example, one effective strategy involves converging many valence (or conduction) bands to achieve a high number of degenerate carrier pockets N_v and hence a high effective mass m^*, resulting in an enhancement of zT in PbTe$_{1-x}$Se$_x$ alloys to about 1.8 at 800 K [6]. Recently, Pei *et al.* have shown [7] that the light band mass leads to higher performance and should be used as an important strategy for discovering and improving thermoelectric materials.

The heavier group-VI element tellurium, which is the main component in many high-performance thermoelectric materials, such as PbTe [5,8,9], Bi$_2$Te$_3$ [10], and AgPbTe$_2$ [11], exhibits a wide variety of interesting properties under pressure and temperature. At ambient pressure, the *twofold* coordinated tellurium has a trigonal crystal structure (Te-I structure) with the $P3_121$-D_3^4 or $P3_221$-D_3^6 space group, depending on the sense of rotation of the helical chains (right- or left-handed screw) [12,13]. This structure, shown in Fig. 1, consists of helical chains, arranged in a hexagonal array, which spiral around axes parallel to the crystalline *c* axis, with three atoms in the unit cell at the positions $(u,0,0)$, $(0,u,\frac{1}{3})$, and $(\bar{u},\bar{u},\frac{2}{3})$. The atomic-position parameter u is related by $u = \frac{q}{a}$ to the radius q of the helices and the lattice constant a [13]. Each atom forms strong covalentlike intrachain bonds with its two nearest neighbors (NNs) and weak van der Waals-like interchain bonds with its four next NNs, thus giving rise to weakly interacting rigid one-dimensional units. This unique feature is in fact reflected in liquid-state studies of Te and Se at atmospheric pressure, indicating that the chain structure is retained above the melting temperature [14].

The twofold coordinated tellurium atoms have unshared electron pairs (lone pairs) which control the interplay of the intra- and interchain interactions and their sensitivity on pressure and temperature. The valence band (VB) sextuplet of Te arises from unhybridized $|p\rangle$ states, i.e., lone pairs, while the doubly degenerate conduction band, protected by the threefold screw symmetry of the helices, is primarily derived from antibonding σ^*-hybridized $|p\rangle$-like states, resulting in a band gap of 0.33 eV [15,16]. More recently we predicted [16] that trigonal tellurium undergoes a trivial insulator to strong topological insulator (metal) transition under shear (hydrostatic or uniaxial) strain. The underlying mechanism is the depopulation of the lone-pair orbitals associated with the VB, which leads to band inversion and the concomitant change of the topological invariant.
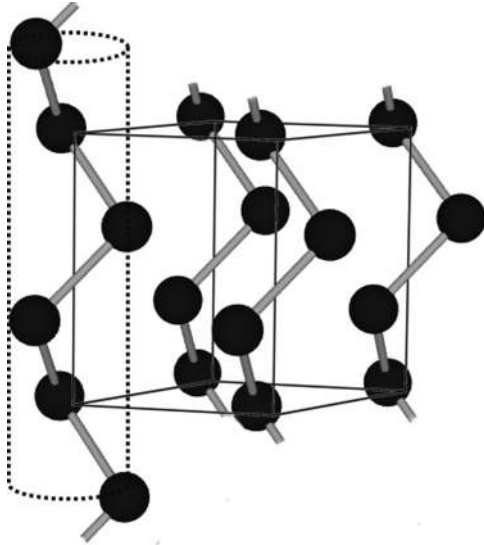
─────────
[*]nick.kioussis@csun.edu

FIG. 1. Trigonal structure of Te-I with the $P3_121$-D_3^4 space group consisting of helical chains arranged in a hexagonal array which spiral around axes parallel to the c axis.

This unique electronic structure of trigonal tellurium invites the intriguing question of the effect of lone pairs in chiral solids on their thermoelectric properties. Furthermore, the addition of 0.2% antimony or bismuth in tellurium increases the conductivity of tellurium by about two orders of magnitude [17]. Thus, if the Sb or Bi doping reduces the lattice contribution to the thermal conductivity, one would expect a high value of zT for elemental bulk tellurium. The objective of this paper is to present a theoretical study of the electronic structure and thermoelectric transport properties of trigonal Te based on *ab initio* density functional calculations and the Boltzmann transport theory.

In Sec. II, we present a brief introduction of the computational methods and various parameters used in the calculations. In Sec. III, we discuss the electronic structures, chemical bonding, and transport properties. We find that the effective mass of the lower valence band along the c axis is low ($0.048m_0$, where m_0 is the electron mass). This in turn contributes to a relatively high room-temperature zT value along the c axis of about 0.31 in hole-doped tellurium with ∼0.001 holes/formula unit. Finally, conclusions are summarized in Sec. IV.

II. COMPUTATIONAL METHOD

To determine the ground-state relaxed atomic structure we have carried out first-principles electronic structure calculations within the framework of the plane-wave projector augmented wave formalism [18], as implemented in the Vienna *ab initio* simulation package (VASP) code without the spin-orbit coupling (SOC) [19,20]. The generalized gradient approximation (GGA) approximation [21] has been employed to treat the exchange-correlation interaction. The plane-wave cutoff energy was 500 eV and the Monkhorst-Pack **k** mesh was $15 \times 15 \times 15$. Ionic and electronic degrees of freedom are relaxed simultaneously until the forces acting on the ions become smaller than 3×10^{-4} eV/Å. We find that the unit cell parameters a and c and the internal atomic position

parameter u are 4.51 Å, 5.96 Å, and $u = 0.269$, in good agreement with the corresponding experimental values of 4.45 Å, 5.93 Å, and 0.263, respectively. However, density functional theory (DFT) studies based on local or semilocal exchange correlation functionals, such as the GGA functional, underestimate the band gap and can lead to an incorrect ordering of the frontier bands at the high symmetry points in the Brillouin zone [22]. Furthermore, they can also give rise to wrong band topologies and effective masses which are crucial in determining accurately the thermoelectric properties [22]. An accurate description of the electronic structure is a prerequisite in the search and discovery efforts for the next-generation thermoelectrics.

Thus, after determining the equilibrium structure, we have carried out electronic structure calculations employing the full-potential WIEN2K code [23] with the SOC included and the modified Becke-Johnson local-density approximation (MBJLDA) functional [24]. The MBJLDA functional has been shown [22] to yield accurate band gaps, effective masses, and frontier-band ordering that are in very good agreement with the computationally more intense GW and hybrid-functional approaches [22]. We used $R_{MT} \times K_{max} = 8.0$, a muffin-tin radius of 2.1 a.u., and a $19 \times 19 \times 12$ **k**-point Monkhorst-Pack mesh.

The transport properties were calculated using the Boltzmann transport theory and the rigid band approach as implemented in the BoltzTraP software [25]. We have employed the eigenenergies on a very dense nonshifted 80 000 **k**-point mesh in the full Brillouin zone (BZ), from the self-consistent converged electronic structure calculations. The electrical conductivity, Seebeck coefficient, and electronic contribution to the thermal conductivity tensors are calculated from [25]

$$\boldsymbol{\sigma} = e^2 \int \boldsymbol{\Xi}(\varepsilon)\left(-\frac{\partial f_0}{\partial \varepsilon}\right)d\varepsilon, \tag{1}$$

$$\boldsymbol{S} = \frac{e}{\boldsymbol{\sigma} T} \int \boldsymbol{\Xi}(\varepsilon)(\varepsilon - \mu)\left(-\frac{\partial f_0}{\partial \varepsilon}\right)d\varepsilon, \tag{2}$$

$$\boldsymbol{\kappa_e} = \frac{1}{T} \int \boldsymbol{\Xi}(\varepsilon)(\varepsilon - \mu)^2\left(-\frac{\partial f_0}{\partial \varepsilon}\right)d\varepsilon. \tag{3}$$

Here, $\Xi^{\alpha,\beta}(\varepsilon) = \sum_{\mathbf{k}} \tau_{\mathbf{k}} \delta(\varepsilon - \varepsilon_{\mathbf{k}}) v_{\mathbf{k}}^\alpha v_{\mathbf{k}}^\beta$ are the matrix elements of the transport distribution function $\boldsymbol{\Xi}$, $v_{\mathbf{k}}^\alpha$ is the αth component of the group velocity of the carriers with wave vector $\mathbf{k}$, and τ is the carrier relaxation time. We have carried out calculations of the transport properties as a function of temperature and chemical potential employing the so-called constant relaxation time approximation (CRTA), which neglects the weak energy dependence of τ but retains some temperature and doping dependence [26,27].

III. RESULTS AND DISCUSSION

The calculated MBJLDA band structure of tellurium with SOC included is shown in Fig. 2(a). The semicore bands (∼−13 to −8 eV) arise primarily from $5|s\rangle$ states, the bonding bands (∼−5 to −2.5 eV) arise from σ hybridization of $5|p\rangle$-like states, and the valence band sextuplet (∼−3 to 0 eV) arises from lone pairs, i.e., unhybridized $5|p\rangle$ states [15,28]. The conduction band sextuplet (∼0 to ∼3 eV) is primarily
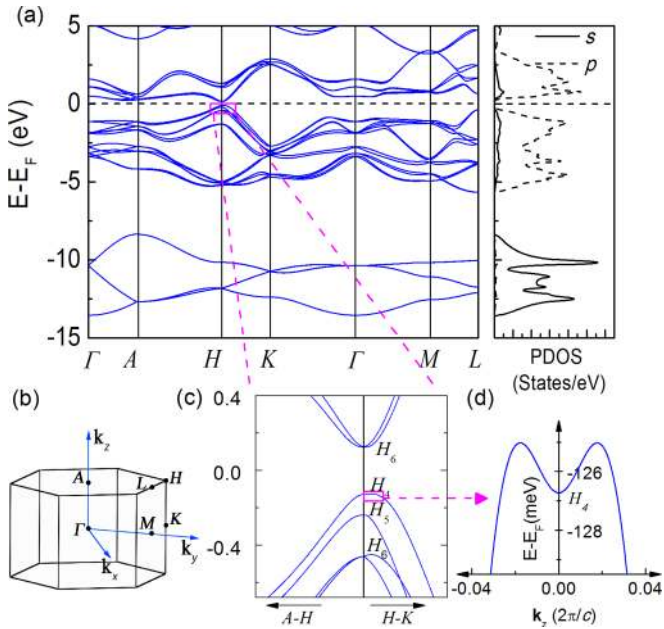
FIG. 2. (Color online) (a) MBJLDA band structure of Te-I with SOC included along the symmetry directions of the Brillouin zone and the corresponding partial (5*s*- and 5*p*-derived) density of states (PDOS). The Brillouin zone of Te-I and the high symmetry **k** points, $\Gamma(0,0,0)$, $A(0,0,1/2)$, $H(1/3,1/3,1/2)$, $K(1/3,1/3,0)$, $M(0,1/2,0)$, and $L(1/2,0,1/2)$. (c) Band structure near the Fermi energy. (d) Valence band in the vicinity of H exhibiting the camelback shape along the H-K (k_z) direction.

FIG. 3. (Color online) (a) Total density of states and (b) the transport distribution function parallel and perpendicular to the *c* axis near the Fermi energy. The inset shows the S-shaped DOS at ~ -0.1 eV below the VBM.

derived from antibonding σ^*-hybridized $|p\rangle$-like states. The total density of states is shown in Fig. 2(a). In the absence of SOC the valence band at $H(\frac{1}{3},\frac{1}{3},\frac{1}{2})$ is fourfold degenerate (H_2). As shown in Fig. 2(c), the SOC splits this band into two nondegenerate H_4 and H_5 valence bands separated by 110 meV and a twofold degenerate lower-energy H_6 band. The calculated H_4-H_5 energy splitting is in agreement with the experimental value of about 112 meV reported in infrared absorption measurements using light polarized parallel to the *c* axis [29]. It is important to emphasize that the lower H_5 valence band close in energy to the upper H_4 valence band gives rise to the S-shape density of states at about 0.1 eV below the valence band maximum (VBM) in Fig. 3(a) and plays an important role in the transport properties. The H_4 upper valence band, shown in Fig. 2(d), exhibits a camelback shape along the H-K (k_z) direction where the valence band maximum in the vicinity of H (hereafter denoted by $\tilde{H}_4$) lies ~ 1.7 meV higher relative to the value at H. This value is in excellent agreement with the value of 1.1 meV reported in infrared absorption measurements [30]. Measurements of the Shubnikov–de Haas effect have also revealed that the Fermi surface of holes in tellurium is of dumbbell shape [31].

The origin of the camelback shape is the SOC which, however, is not large enough to cause inversion between the frontier bands. On the other hand, shear strain leads to depopulation of the lone-pair orbitals of the upper lone-pair derived valence band (H_4), rendering the system a strong topological insulator [16]. The importance of the camelback-shape top valence band is that it increases the number of the
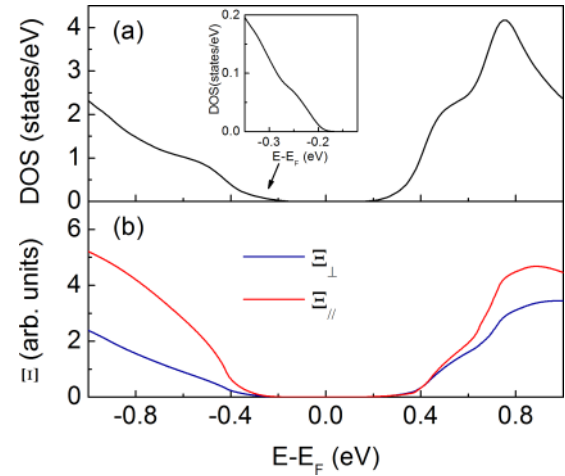
degenerate hole pockets, which in turn increases the density of states effective mass. The twofold degenerate conduction band at H is of H_6 symmetry. The calculated MBJLDA indirect band gap of 0.25 eV in the vicinity of the H point is in good agreement with the experimental value of 0.33 eV [32]. Note that the band gap of Te fulfills the optimum band gap criterion for a high-performance thermoelectric at 300 K [33].

The effective mass $m^* = N_v^{3/2} m_b^*$ [34] near the Fermi energy is an important parameter for the thermoelectric transport. Here, N_v is the degeneracy of the band, and m_b^* is the effective mass of a single valley. A higher effective mass is beneficial for a high Seebeck coefficient. On the other hand, since the carrier mobility is inversely proportional to the effective mass, $\mu \propto (m_b^*)^{-3/2}(m_c^*)^{-1/2}$ (m_c^* is the effective mass along the conducting direction), the overall electronic transport performance $S^2\sigma \propto N_v(m_c^*)^{-1}$ is inversely proportional to m_c^*. Consequently, a small effective mass and a large band degeneracy are the most important factors to achieve high thermoelectric performance [2,7]. We find that the band structure of trigonal tellurium satisfies these criteria. Table I lists the calculated hole effective masses parallel and perpendicular to the *c* axis at the maximum of the uppermost

TABLE I. The calculated MBJLDA band effective masses (in units of the free-electron mass m_0) parallel, $(m_b^*)_\parallel$, and perpendicular, $(m_b^*)_\perp$, to the *c* axis for the valence band maximum in the vicinity of H_4 ($\tilde{H}_4$), the lower valence band maximum (H_5), and the conduction band (H_6) at H, respectively. For comparison, we also list the corresponding experimental values.

	$\tilde{H}_4$		H_5		H_6	
	Calc.	Expt.[a]	Calc.	Expt.[a]	Calc.	Expt.[b]
$(m_b^*)_\parallel$	0.251	0.220	0.048	0.039	0.073	0.070
$(m_b^*)_\perp$	0.098	0.108	0.223	0.256	0.108	0.104

[a]Reference [35].
[b]Reference [36].

and lower valence bands, and the electron effective masses at the conduction band minimum (CBM). For comparison we also list the corresponding experimental values [35,36]. The bands near the Fermi level in Fig. 2(c) show significant anisotropic behavior. The uppermost valence band along the H-A symmetry direction ($k_\perp$) is more dispersive than that along the H-K symmetry direction ($k_\parallel$), yielding an effective mass perpendicular to the c axis, $(m_b^*)_\perp = 0.098 m_0$, smaller than that of VBM parallel to the c axis, $(m_b^*)_\parallel = 0.251 m_0$.

The upper (H_4) and lower (H_5) lone-pair derived valence bands, which are the primary bands for hole transport, also differ greatly in their dispersion relation. We find that for the lower valence band, $(m_b^*)_\perp = 0.223 m_0$ and $(m_b^*)_\parallel = 0.048 m_0$, respectively. Interestingly, the effective mass of the H_5 valence band along the chain direction is smaller than that of the H_4 band. Overall, the small effective masses contribute to a higher hole mobility and hence large electrical conductivity. Furthermore, the number of degenerate hole pockets along the H-K direction in the vicinity of the valence band maximum is $N_v = 4$. This in turn increases the density of states effective mass m^*, which is beneficial for a larger Seebeck coefficient. Both the upper and lower valence bands contribute to the transport as the chemical potential shifts to lower energies through p-type doping (Bi or Sb doping), resulting in a large Seebeck coefficient. It is important to note that the underlying mechanism for the high zT in tellurium is the light effective masses (if one neglects the scattering process), consistent with the recent proposal of Pei et $al.$ for PbTe [7].

Figures 3(a) and 3(b) show the calculated density of states (DOS) and the transport distribution function of tellurium, respectively. Interestingly, we find that the DOS of the three-dimensional tellurium displays a staircaselike shape (S shape) characteristic of two-dimensional (2D) materials [1]. This type of DOS increases the asymmetry of the transport distribution function Ξ in (2) and hence the Seebeck coefficient. The first staircase which appears at an energy of $\sim$0.1 eV below the VBM is due to the contribution from the lower valence band (H_5), which results in an increase of the DOS effective mass and the asymmetry of Ξ. Similarly, the DOS of the conduction band exhibits a staircaselike shape at $\sim$0.3 eV above the Fermi energy arising from the flat conduction band along the Γ-A symmetry direction, giving rise to a large band effective mass. This in turn enhances the Seebeck coefficient, albeit at the expense of the electrical conductivity. The transport distribution function which contains the contributions from both the group velocity and the density of states shows that $\Xi_\parallel > \Xi_\perp$ and $\frac{d\Xi_\parallel}{dE} > \frac{d\Xi_\perp}{dE}$ for the valence bands, which is beneficial to both the electrical conductivity and the Seebeck coefficient along the chains.

We performed calculations of the transport properties as a function of carrier concentration and temperature within the CRTA. The CRTA has been successfully applied to many thermoelectric materials, including degenerately doped semiconductors, Zintl-type phases, and oxides [26,27]. Within the CRTA, τ is exactly canceled in the expression (2) of the Seebeck coefficient. Thus, within this approximation, the thermopower can be directly evaluated from the first-principles band structures. On the other hand, the evaluation of the electronic conductivity in (1) and the electronic contribution to the thermal conductivity in (3) requires knowledge of τ,
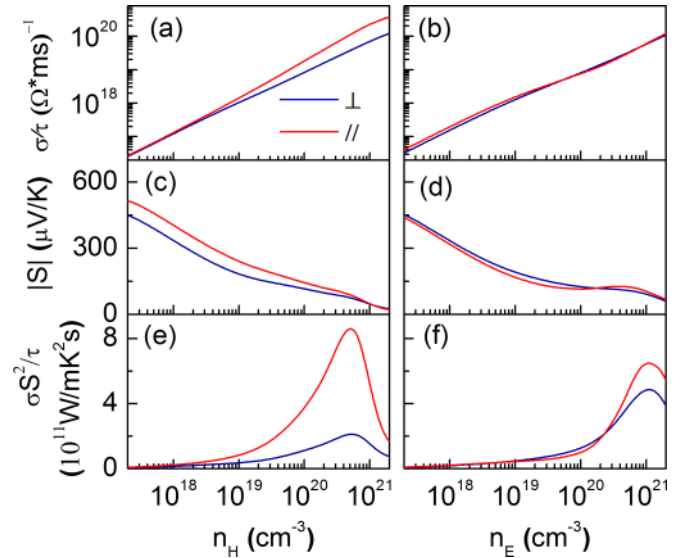

FIG. 4. (Color online) Calculated transport coefficients (a), (b) σ/τ, (c), (d) S, and (e), (f) $S^2\sigma/\tau$ parallel and perpendicular to the c axis vs carrier concentration for p- (left panels) and n-type (right panels) doped tellurium at 300 K.

which is often taken from experiment. The effect of doping is simulated using the rigid band model, which assumes that light doping does not change the shape of the band structure, but only shifts the Fermi energy.

The left (right) panels in Fig. 4 show the transport coefficients parallel and perpendicular to the c axis as a function of the hole (electron) concentration at $T = 300$ K. As can be seen in Figs. 4(a) and 4(b), the σ/τ increases with increasing carrier concentration while the magnitude of S in Figs. 4(c) and 4(d) decreases with doping. The conductivity (σ/τ) in Fig. 4(a) exhibits an anisotropic behavior with $(\sigma/\tau)_\parallel > (\sigma/\tau)_\perp$ at a hole concentration higher than 2×10^{18} cm^{-3}. This is due to the large contribution to the electrical conductivity σ/τ from the lower valence band H_5, which is about 0.11 eV below the H_4 uppermost valence band and has a very small hole effective mass along the c axis. We should note that the rigid band approach most probably fails at high carrier concentrations ($>10^{20}$ cm^{-3}).

The calculated Seebeck coefficients along and perpendicular to the chain axis as a function of carrier concentration are shown in Figs. 4(c) and 4(d) for p- and n-type doping, respectively, at 300 K. We find a large asymmetry of the Seebeck coefficient along and perpendicular to the c axis for p-type doped tellurium where $S_\parallel/S_\perp \sim 1.25$ at a hole concentration about 10^{19} cm^{-3}. It is important to note that the Seebeck coefficients for both n- and p-type doped tellurium are quite large at room temperature, reaching a peak value of 450 μV/K at a hole concentration around 10^{17} cm^{-3} and with an average value in the range of 200–250 μV/K. These values of S for a single-element solid compare favorably with those reported for optimized Bi$_2$Te$_3$ [37]. The large Seebeck coefficient for tellurium is mainly due to the large asymmetry of the transport distribution function from the the staircaselike DOS shown in Fig. 3(a). For the p-type doped tellurium, the staircaselike DOS arises from the contribution of the lower
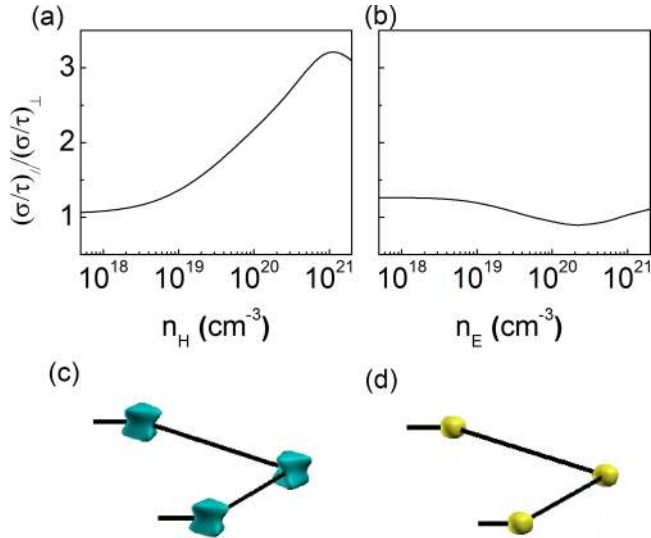
FIG. 5. (Color online) Ratio of $(\sigma/\tau)_\parallel$ and $(\sigma/\tau)_\perp$ as a function of carrier concentration at 300 K for (a) p-type and (b) n-type doped tellurium. The Fermi surfaces at (c) 0.06 eV below the VBM and (d) 0.06 eV above the CBM.
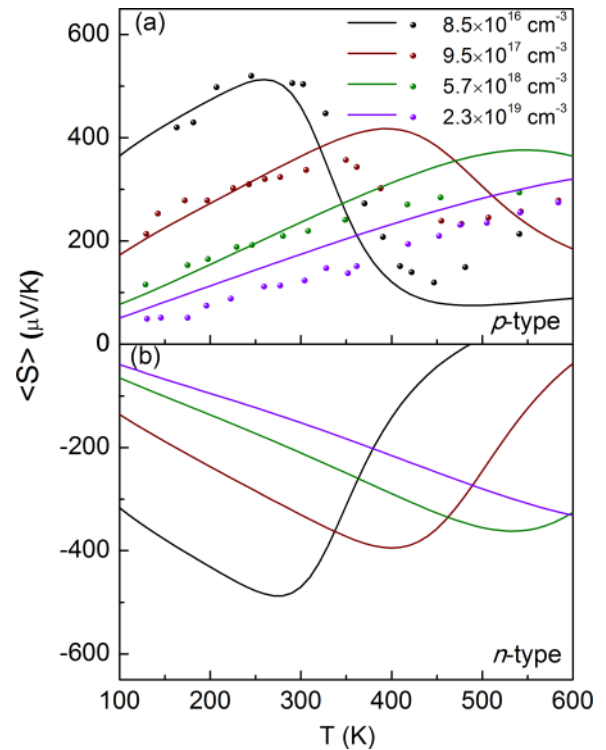

FIG. 6. (Color online) Temperature dependence of the calculated (solid curves) average Seebeck coefficient, $\langle S \rangle = (S_{xx}\sigma_{xx} + S_{yy}\sigma_{yy} + S_{zz}\sigma_{zz})/(\sigma_{xx} + \sigma_{yy} + \sigma_{zz})$, for various carrier concentrations for p- and n-type doped tellurium. For the p-type doping, for comparison, we also show the experimental results (circles).

valence bands, which is similar to superlattice systems where the asymmetry arises from the contribution of the various minibands. In contrast, for n-type doped tellurium, the increase in DOS is due to the increase of the band effective mass as the chemical potential shifts above the conduction band minimum. This in turn increases the Seebeck coefficient, albeit not beneficially for the electrical conductivity.

Figures 4(e) and 4(f) show the power factor $S^2\sigma/\tau$ at 300 K parallel and perpendicular to the chain axis for p- and n-doped tellurium, respectively. The results show a larger anisotropy in the power factor for the p-type carriers compared to that for the n type. For p-type doped tellurium $(S^2\sigma/\tau)_\parallel$ is about three times larger than $(S^2\sigma/\tau)_\perp$ around 10^{19} cm^{-3}. The power factor anisotropy arises from the large and different anisotropy of the conductivity and Seebeck coefficient for p and n types, as described above.

The anisotropic behavior of (σ/τ) associated with band structure is shown in Fig. 5(a), where we plot the ratio $\frac{(\sigma/\tau)_\parallel}{(\sigma/\tau)_\perp}$ as a function of carrier concentration at 300 K. We find that this ratio is ~ 1 for n-type doped tellurium, indicating that the electron transport is isotropic if one neglects the scattering factor. In contrast, this ratio can reach about 3 in p-type doped tellurium, indicating that the hole transport is anisotropic where the effective hole transport takes place primarily along the chains. This anisotropic difference can be understood from the Fermi surfaces shown in Figs. 5(c) and 5(d). The Fermi surface at 0.06 eV above the CBM shows that the electron pockets are almost spherical. On the other hand, the Fermi surface at 0.06 eV below the VBM shows that the hole pockets have an ellipsoidal shape.

Figure 6 shows the temperature dependence of the average Seebeck coefficient, $\langle S \rangle = (S_{xx}\sigma_{xx} + S_{yy}\sigma_{yy} + S_{zz}\sigma_{zz})/(\sigma_{xx} + \sigma_{yy} + \sigma_{zz})$, for the hole- and electron-doped tellurium, respectively, for various carrier concentrations. For the hole-doped system we also show for comparison the exper-

imental data (circles) for the antimony-doped tellurium [38]. Since tellurium has a small band gap, the contribution of the thermally activated minority carriers to the Seebeck coefficient compensates that from the majority carriers. Thus, at low carrier concentration, tellurium exhibits a bipolar effect which becomes weaker as the carrier concentration increases. The n-type tellurium has a larger bipolar effect than the p type, where at low carrier concentration the Seebeck coefficient changes sign with increasing temperature. Overall, the results of the *ab initio* calculations are in good agreement with experiment except in the high temperature region, which is due presumably to the reduction of the band gap with increasing temperature.

The calculation of the power factor and zT as a function of hole concentration and temperature requires knowledge of the concentration- and temperature-dependent relaxation times parallel, $\tau_\parallel(n_H, T)$, and perpendicular, $\tau_\perp(n_H, T)$, to the c axis. These are determined from $\tau_{\parallel(\perp)} = \frac{|e|n_H\mu_{\parallel(\perp)}^{\text{expt.}}}{(\frac{\sigma}{\tau})_{\parallel(\perp)}^{\text{theor}}}$, where n_H is the concentration of holes, $\mu_{\parallel(\perp)}^{\text{expt.}}$ is the experimentally determined [38,39] concentration- and temperature-dependent mobility parallel and perpendicular to the chains, and $(\frac{\sigma}{\tau})_{\parallel(\perp)}^{\text{theor}}$ is calculated from (1). Since the available experimental data for $\mu_{\parallel(\perp)}^{\text{expt.}}(n_H, T)$ is limited to $T = 300$ K, assuming that the mobility is dominated by phonon scattering where its temperature dependence is proportional to $T^{-3/2}$, we have determined also the mobility and the relaxation times at 500 K. The hole concentration dependence of $\tau_{\parallel(\perp)}$ at $T = 300$ and 500 K is shown in the insets of Figs. 7(a) and 7(b), respectively.
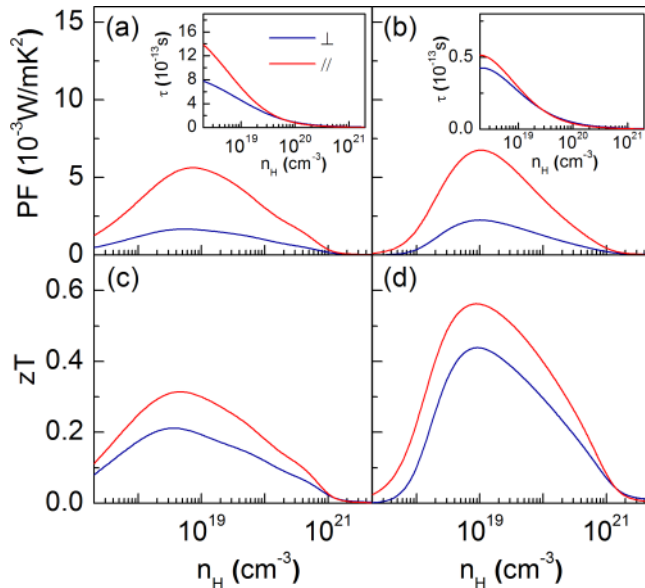
FIG. 7. (Color online) The calculated (a), (b) power factor and (c), (d) zT of tellurium parallel (red) and perpendicular (blue) to the c axis vs hole concentration at room temperature and 500 K. The insets show the concentration dependence of the relaxation times parallel and perpendicular to the chains at 300 and 500 K, respectively.

For the calculation of the figure of merit zT we have taken into account the contributions of both the lattice thermal conductivity $\kappa_L(T)$ and the electronic thermal conductivity $\kappa_e(n_H, T)$ to the total thermal conductivity parallel and perpendicular to the c axis. The concentration- and temperature-dependent electronic thermal conductivity is obtained using the Boltzmann transport expression (3). At a low hole concentration of 2×10^{17} cm^{-3} we find that the room-temperature electronic thermal conductivity perpendicular and parallel to the c axis is 0.19 and 0.49 W m^{-1} K^{-1}, respectively. At a higher hole concentration of 6×10^{18} cm^{-3} the room-temperature electronic thermal conductivity perpendicular and parallel to the c axis is ~0.87 and 2.5 W m^{-1} K^{-1}, respectively. On the other hand, the lattice contribution to the thermal conductivity is taken from experiment [40]. The room-temperature lattice thermal conductivity perpendicular and parallel to the c axis is 1.6 and 2.9 W m^{-1} K^{-1}, respectively. In the absence of experimental data for the thermal conductivity at 500 K we have employed the $1/T$ temperature dependence of $\kappa_L(T)$ and extrapolated to higher temperatures. Figure 7 shows the hole concentration dependence of the power factor and zT parallel and perpendicular to the chain axis at 300 and 500 K, respectively. At room temperature, the power factor can reach

a value as high as about 5 mW/mK^2. Note that for p-type doped tellurium with a carrier concentration of 6×10^{18} cm^{-3}, the room-temperature zT along the c axis is 0.31, which is comparable to the maximum room-temperature value of 0.6 for Bi$_2$Te$_3$ if one considers only the doping effect [26]. At 500 K, zT can reach the maximum value of about 0.56 at a hole concentration of 1×10^{19} cm^{-3}. It is important to emphasize that if the lattice thermal conductivity of tellurium is reduced though doping with Bi or Sb or the bipolar effect is reduced through nanostructure engineering [41], the zT of Te p-doped alloys could be even further enhanced, rendering them promising materials for thermoelectric applications.

IV. CONCLUSION

The electronic structure and thermoelectric transport properties of tellurium have been investigated by DFT and the Boltzmann transport theory. We find that, overall, the electrical conductivity, Seebeck coefficient, and figure of merit of p-doped tellurium parallel to the helical chains are much higher than those perpendicular to the chains due to the anisotropy of the hole pockets. The underlying origin lies on the complex electronic structure consisting of (i) the heavy-hole uppermost (H_4) and extremely light-hole lower (H_5) *lone-pair* derived valence bands contributing to both the high Seebeck coefficient and the electrical conductivity, and (ii) the stairlike DOS yielding a large asymmetry for the transport distribution function relative to the Fermi level, which is beneficial for large thermopower. The average Seebeck coefficient at room temperature of about 250 μV/K is comparable to that of Bi$_2$Te$_3$. The optimum zT of p-type doped tellurium is 0.31 at room temperature and 0.56 at 500 K at the optimum hole concentration around 1×10^{19} cm^{-3} via Sb or Bi doping. More importantly, such doping can reduce the lattice thermal conductivity and hence further enhance zT. Current work is aimed at employing a first-principles theoretical approach to calculate the lattice thermal conductivity of tellurium based on a solution of the Boltzmann transport equation with a relaxation time approximation. These results pave the way towards opportunities for developing chiral-based polychalcogenide thermoelectric materials and we hope they inspire further experimental explorations.

[1] M. S. Dresselhaus, G. Chen, M. Y. Tang, R. G. Yang, H. Lee, D. Z. Wang, Z. F. Ren, J. P. Fleurial, and P. Gogna, Adv. Mater. **19**, 1043 (2007).

[2] G. J. Snyder and E. S. Toberer, Nat. Mater. **7**, 105 (2008).

[3] J. R. Sootsman, D. Y. Chung, and M. G. Kanatzidis, Angew. Chem. Int. Ed. **48**, 8616 (2009).

[4] L. D. Hicks and M. S. Dresselhaus, Phys. Rev. B **47**, 12727 (1993).

[5] J. P. Heremans, V. Jovovic, E. S. Toberer, A. Saramat, K. Kurosaki, A. Charoenphakdee, S. Yamanaka, and G. J. Snyder, Science **321**, 554 (2008).

[6] Y. Pei, X. Shi, A. LaLonde, H. Wang, L. Chen, and G. J. Snyder, Nature (London) **473**, 66 (2011).

[7] Y. Pei, A. D. LaLonde, H. Wang, and G. J. Snyder, Energy Environ. Sci. **5**, 7963 (2012).

[8] Y. Pei, H. Wang, and G. J. Snyder, Adv. Mater. **24**, 6125 (2012).

[9] K. Biswas, J. He, I. D. Blum, C.-I. Wu, T. P. Hogan, D. N. Seidman, V. P. Dravid, and M. G. Kanatzidis, Nature (London) **489**, 414 (2012).

[10] O. Yamashita, S. Tomiyoshi, and K. Makita, J. Appl. Phys. **93**, 368 (2003).

[11] D. T. Morelli, V. Jovovic, and J. P. Heremans, Phys. Rev. Lett. **101**, 035901 (2008).

[12] J. Donohue, *The Structures of the Elements* (Wiley, New York, 1974).

[13] R. Keller, W. B. Holzapfel, and H. Schulz, Phys. Rev. B **16**, 4404 (1977).

[14] B. C. Deaton and F. A. Blum, Jr., Phys. Rev. **137**, A1131 (1965).

[15] F. Kirchhoff, N. Binggeli, G. Galli, and S. Massidda, Phys. Rev. B **50**, 9063 (1994).

[16] L. A. Agapito, N. Kioussis, W. A. Goddard, III, and N. P. Ong, Phys. Rev. Lett. **110**, 176401 (2013).

[17] C. H. Cartwright and M. Haberfeld, Nature (London) **134**, 287 (1934).

[18] P. E. Blöchl, Phys. Rev. B **50**, 17953 (1994).

[19] G. Kresse and J. Furthmüller, Phys. Rev. B **54**, 11169 (1996).

[20] G. Kresse and J. Furthmüller, Comput. Mater. Sci. **6**, 15 (1996).

[21] J. P. Perdew, K. Burke, and M. Ernzerhof, Phys. Rev. Lett. **77**, 3865 (1996).

[22] Y.-S. Kim, M. Marsman, G. Kresse, F. Tran, and P. Blaha, Phys. Rev. B **82**, 205212 (2010).

[23] P. Blaha, K. Schwarz, G. K. H. Madsen, D. Kvasnicka, and J. Luitz, *WIEN2k, An Augmented Plane Wave + Local Orbitals Program for Calculating Crystal Properties* (Karlheinz Schwarz, Technische Universität, Wien, Austria, 2001).

[24] F. Tran and P. Blaha, Phys. Rev. Lett. **102**, 226401 (2009).

[25] G. K. H. Madsen and D. J. Singh, Comput. Phys. Commun. **175**, 67 (2006).

[26] D. Parker and D. J. Singh, Phys. Rev. X **1**, 021005 (2011).

[27] L. Xi, Y. B. Zhang, X. Y. Shi, J. Yang, X. Shi, L. D. Chen, W. Zhang, J. Yang, and D. J. Singh, Phys. Rev. B **86**, 155201 (2012).

[28] M. Kastner, Phys. Rev. Lett. **28**, 355 (1972).

[29] R. S. Caldwell and H. Y. Fan, Phys. Rev. **114**, 664 (1959).

[30] T. Doi, K. Nakao, and H. Kamimura, J. Phys. Soc. Jpn. **28**, 822 (1970).

[31] C. Guthmann and J. M. Thuillier, Solid State Commun. **6**, 835 (1968).

[32] V. B. Anzin, M. I. Eremets, Y. V. Kosichkin, A. I. Nadezhdinskii, and A. M. Shirokov, Phys. Status Solidi A **42**, 385 (1977).

[33] J. O. Sofo and G. D. Mahan, Phys. Rev. B **49**, 4565 (1994).

[34] G. D. Mahan, *Solid State Physics*, edited by H. Ehrenreich and F. Spaepen (Academic, New York, 1998), Vol. 51, p. 81.

[35] Y. Couder, M. Hulin, and H. Thomé, Phys. Rev. B **7**, 4373 (1973).

[36] H. Shinno, R. Yoshizaki, S. Tanaka, T. Doi, and H. Kamimura, J. Phys. Soc. Jpn. **35**, 525 (1973).

[37] L. M. Goncalves, C. Couto, P. Alpuim, A. G. Rolo, F. Völklein, and J. H. Correia, Thin Solid Films **518**, 2816 (2010).

[38] T. Fukuroi, S. Tanuma, and S. Tobisawa, Sci. Rep. Res. Inst., Tohoku Univ., Ser. A **4**, 283 (1952).

[39] P. Grosse, in *The Physics of Tellurium*, Springer Tracts in Modern Physics, Vol. 48 (Springer, Berlin, 1969).

[40] A. R. Adams, F. Baumann, and J. Stuke, Phys. Status Solidi B **23**, K99 (1967).

[41] A. J. Minnich, M. S. Dresselhaus, Z. F. Ren, and G. Chen, Energy Environ. Sci. **2**, 466 (2009).